

Regional Variability of Rain Clouds in the Amazon Basin as Seen by a Network of Weather Radars

I. SARAIVA

Meteorology Division, Regional Center of Manaus, Operations and Management Center of the Amazonian Protection System, and Graduate Program in Climate and Environment, National Institute for Amazonian Research, Manaus, Brazil

M. A. F. SILVA DIAS AND C. A. R. MORALES

Department of Atmospheric Sciences, University of São Paulo, São Paulo, Brazil

J. M. B. SARAIVA

Meteorology Division, Regional Center of Manaus, Operations and Management Center of the Amazonian Protection System, Manaus, Brazil

(Manuscript received 24 June 2015, in final form 16 September 2016)

ABSTRACT

A new dataset based on 5 yr of operational meteorological weather radars from the Amazon Protection System has enabled new knowledge in relation to rainfall in the Amazon basin. The rainy features are analyzed for 10 different regions in terms of the annual and diurnal cycles of radar reflectivity, as well as the vertical distribution, in addition to lightning data. Similarities between the annual and diurnal cycles are found in the northwestern and western, southwestern and southern, and northeastern and northern Amazon. Nocturnal peaks are found in stratiform fraction in the southern, southwestern, western, northwestern, northern, central western, and coastal regions. The convective fractions in the western, northwestern, northern, and central eastern regions also show nocturnal peaks. The radar reflectivity vertical distributions analysis indicates that in the northern coast close to Belém, heavy rainfall with deep convective systems is observed throughout the year, while heavy rainfall in the central Amazon close to Manaus, Tefé, and Santarém occurs in the dry season. More oceanic-like clouds are also observed there and in other locations on the northern coast like Macapá, where the frequency of lightning is quite low. São Gabriel da Cachoeira, located in the northwest portion of the Amazon basin, has a regime with rainfall in all seasons with a slight decrease from August to October when the systems become more convective and have more lightning.

1. Introduction

The Amazon basin spreads from 5°N to 18°S and from 42° to 74°W, with an area of about 7 million km². Different rainfall climatology (e.g., Rao and Hada 1990) has been reported in several subregions of the Amazon related to the influence of different weather systems. In the north, the intertropical convergence zone (ITCZ) and Atlantic easterly waves dominate the regional climate, while in the southern region weak frontal systems as well as stationary fronts such as the South Atlantic convergence zone (SACZ) provide the framework for

rainfall development (Satyamurty et al. 1998). Meso-scale convective systems (MCSs) have been observed over all the Amazon (Greco et al. 1990; Machado et al. 1998; Silva Dias et al. 2009b) and in particular in the form of squall lines originating on the northern coast (Cohen et al. 1995). To the west of the basin, the Andes Mountains provide a barrier for the northeasterly trades coming from the equatorial Atlantic. On the eastern slopes of the Andes, topographical uplift is associated with very high annual amounts of accumulated rainfall in excess of 3500 mm (Figueroa and Nobre 1990).

Most striking of all, the Amazon rain forest is the main land-cover feature in the central and northwestern regions, while deforestation areas, savannah-type vegetation, and agriculture are mainly on the southern and

Corresponding author e-mail: Ivan Saraiva, ivan.saraiva@sipam.gov.br

eastern edges of the forest (Ter Steege et al. 2013). The process of deforestation is associated with biomass burning in the dry season releasing an enormous amount of aerosol into the atmosphere (Artaxo et al. 2002). Several studies have pointed to an impact on rainfall due to biomass burning (e.g., Andreae et al. 2004; Albrecht et al. 2011). Other studies have pointed to the effect of deforestation on rainfall patterns and intensities (Saad et al. 2010; Silva Dias et al. 2009a).

Past studies of rainfall in the Amazon basin have relied on rain gauge analysis (e.g., Rao and Hada 1990), satellite-derived rainfall (Negri et al. 1994, 2002), or combinations of satellite and rain gauge (e.g., Buarque et al. 2011). Rain features based on the Tropical Rainfall Measuring Mission Precipitation Radar (TRMM PR; e.g., Liu et al. 2008) have been used to provide a larger-scale view, but it is still limited by temporal resolution that prevents the analysis in the time scale of cloud lifetime. Several field campaigns conducted in the region since the 1980s have provided case studies of clouds and rainfall for limited periods of time with enhanced resources such as ground-based weather radars, lidars, rain gauges, and disdrometers (Silva Dias et al. 2002; Machado et al. 2014). The several studies mentioned here combine to suggest a picture where regional heterogeneity is the dominant feature.

The regional features of rain clouds that have been seen in previous studies certainly need further analysis with a more consistent and widespread dataset. One important issue is to describe the character of clouds as being convective or stratiform, evaluate their annual and diurnal variability, and indicate possible causes of the observed behavior. The expected results are useful in the sense that models still lack a good representation of rainfall in tropical regions (e.g., Bechtold et al. 2004) and also because most of the model results have only been validated in regions where data are available. There is no guarantee that a validation in a particular region will work for another subregion, especially in the case of the Amazon basin where there is a transition from equatorial to tropical and from coastal to continental regimes.

Several authors (Albrecht et al. 2011; Anagnostou and Morales 2002; Carvalho et al. 2002; Rickenbach et al. 2002; Williams et al. 2002; Petersen et al. 2002) have investigated the relationship of low-level wind to the more convective or stratiform portions of rain cloud systems. However, this was mainly focused on the wet season in the southwest Amazon where the TRMM-LBA campaign took place (Silva Dias et al. 2002). Basically, two regimes were identified: the westerly regime, where monsoon-type systems were associated with larger stratiform area fractions, and break regimes, in

which low-level easterly winds were associated with larger convective area fraction. These analyses were possible for the 2-month field campaign mainly because there were data provided by radars. But can we generalize this for other areas within the Amazon basin? Certainly the system that provided the large-scale situation in the southwest Amazon affects other areas in a different way.

Another aspect that has been studied for some time has been the potential effect of aerosols due to biomass burning on the evolution of rain clouds in the Amazon. The transition seasons, mainly between the dry and wet seasons, have been the focus of most of this research. From a modeling point of view, Martins et al. (2009) show that aerosols may invigorate rain clouds, making them deeper, with stronger updrafts and downdrafts. However, from the point of view of observations there are controversies. This issue has been part of the objectives of several field campaigns, and the discussion has been on the possible role of a large-scale situation that inhibits cloud development and on the role of the aerosol loading that may affect cloud microphysics (Rosenfeld and Silva Dias 2008; Albrecht et al. 2011). Andreae et al. (2004) show different cloud structures in different air masses with contrasting aerosol loadings.

It is clear from this brief summary that understanding rainfall in the Amazon basin is still a challenging subject, and more data are necessary. With this perspective, a new database based on 5 yr of weather radar operations of the Amazon Protection System [Sistema de Proteção da Amazônia (SIPAM)], run by the Brazilian Air Force, brings new possibilities and insights. The objective of this paper is to describe this new dataset, present the calibration performed, and show general features of rain clouds seen by the 10 weather radars that distinguish the different rainfall regimes of the Amazon basin. The results may be seen as preliminary in the sense that five years are not sufficient to define a climatology. However, they point to interesting regional features that should motivate further research. In section 2, the data are described and calibration of radar reflectivity is introduced, section 3 presents the methodology, section 4 presents and discusses the results, and section 5 draws the conclusions. The SIPAM dataset is available online (<http://www.sipam.gov.br/novo-contato>), and the subsets used in this paper are available from the authors upon request.

2. Data

The database compiled in this study represents the continuous 240-km volume scan (VOLSCAN) of 10 meteorological weather radars shown in Fig. 1 that cover the Amazon basin. The SIPAM weather radars are Doppler and S-band, and have a 4.2-m-diameter

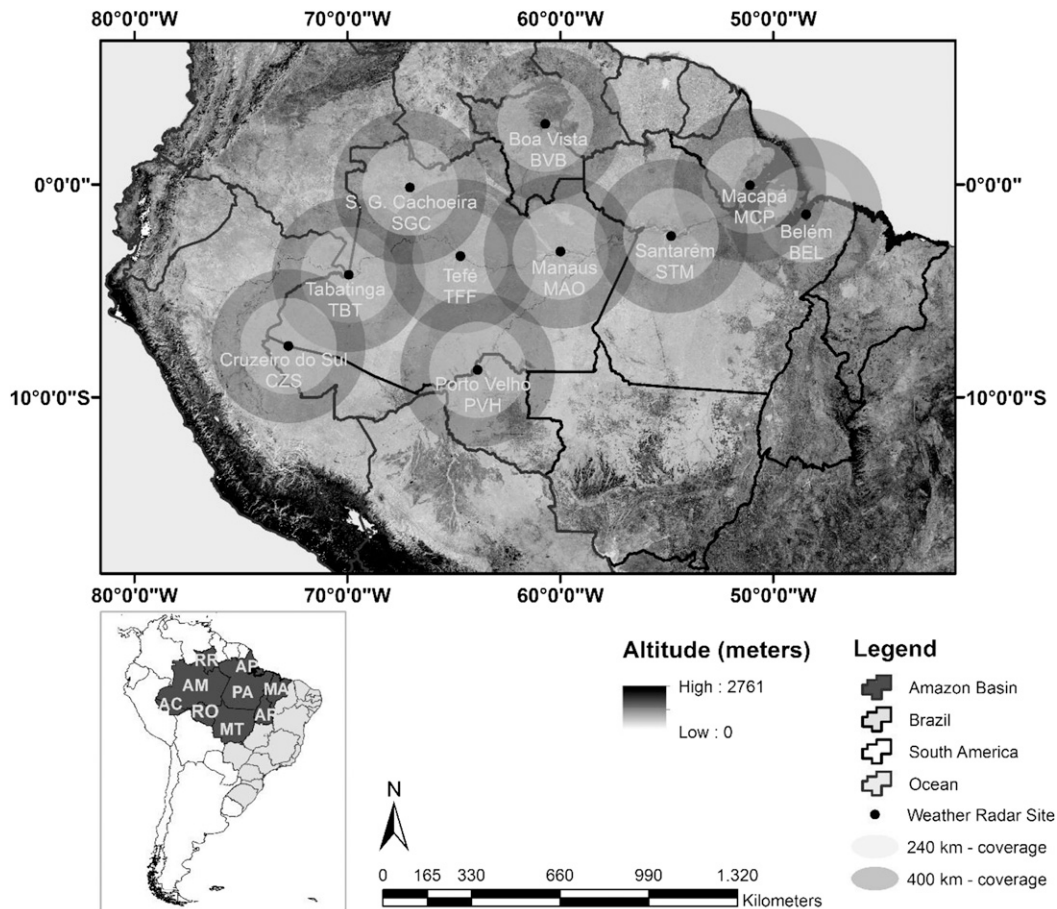


FIG. 1. Coverage of the SIPAM meteorological radars located along the Amazon in Brazil. Shading is topography in meters.

antenna with a beamwidth of 1.8° . The data used here refer to the period of 5 yr starting on 1 January 2008 and ending on 31 December 2012.

The radars are named as follows:

- São Gabriel da Cachoeira (SGC), Tabatinga (TBT), Tefé (TFF), and Manaus (MAO), in the state of Amazonas;
- Cruzeiro do Sul (CZS) in the state of Acre;
- Porto Velho (PVH) in the state of Rondônia;
- Boa Vista (BVB) in the state of Roraima;
- Macapá (MCP) in the state of Amapá; and
- Belém (BEL) and Santarém (STM) in the state of Pará.

The ground radar (GR) VOLSCANs were calibrated against TRMM PR as described in a later section. TRMM PR provides 49 vertical profiles every scan with a gate resolution of 250 m, with 4.5-km resolution at the surface (Kummerow et al. 1998). The calibration procedure uses TRMM PR attenuation corrected reflectivity data given by the algorithm 2A25 (Iguchi and Meneghini 1994).

An independent dataset is used to analyze the intensity of rainfall systems across the Amazon region: the lightning data obtained by the Sferics Timing and Ranging Network (STARNET) described by Morales et al. (2011). STARNET is a long-range network for lightning detection that uses radio noise emitted by atmospheric discharges known as sferics. The system uses very low frequency (VLF) radio antennas and measures the vertical electric field in the range of 7–15 kHz. STARNET can detect up to 100 sferics per second that are located by employing the arrival time difference (Lee 1986). According to Morales et al. (2011), the system is able to measure sferics in most of South America with a precision of 2–10 km and a sferics detection efficiency of 50%–70%.

The following sections describe the operational strategy of the GR data acquisition, the data that are included in the database, and the calibration procedure performed.

a. Operational acquisition strategy

The SIPAM radars are Doppler Weather System Radar (DWSR) 8500S manufactured by Enterprise

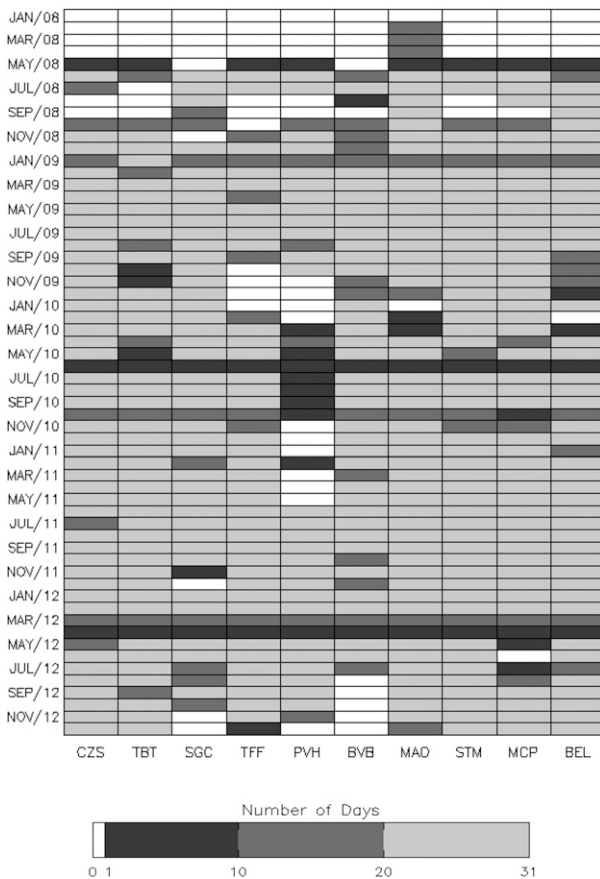


FIG. 2. Number of days in each month from 2008 to 2012 in which the volume scan of each SIPAM radar is stored in the database.

Electronics Company that were integrated by the radar control computer software from Gesellschaft für Angewandte Mikrowellen- und Informationstechnologie und Consulting (GAMIC; Malkomes et al. 2002) to be consistent with the six other weather radars from the Department of Airspace Control [Departamento de Controle do Espaço Aéreo (DECEA)] of Brazil. Recently, the 11th SIPAM weather radar has been installed in São Luís, Maranhão. This radar will not be studied in this article since there is not enough information in the database. The SIPAM radar network operates in partnership with DECEA, which is responsible for the physical maintenance of the radars. The corrective and preventive maintenance and data transmission require significant effort on the institutions involved, since transportation and communication in the Amazon region are complicating factors for the system functioning. However, the network has been operating since 2002, and after 2008 it began to store the volumetric data.

SIPAM weather radars are configured to perform two types of volumetric scans. The first scan, defined as meteorological, covers 240 km with a gate resolution of

500 m, PRF of 621 Hz, and antenna speed of 2.5 rpm with 17 elevations (0.9° bottom and 19.5° top elevation angles). The second scan, defined as surveillance, targets the 400-km range with a gate resolution of 500 m, PRF of 350 Hz, and antenna speed of 2.5 rpm with three elevations (0.9° bottom and 3.7° top elevation angles). With the present configuration the radars perform two scans every 12 min. Before July 2008, the temporal resolution was 10 min. Every VOLSCAN includes uncorrected radar reflectivity, corrected radar reflectivity Z , radial velocity, and spectral width. For this study, the analysis concentrates only on Z data from meteorological VOLSCANS.

Based on the fact that these weather radars have a beamwidth of 1.8° , with an azimuth sample of 1° and a gate resolution of 500 m, we have limited the 3D rainfall representation up to 150 km from the GR. Thus, for the study we computed constant-altitude plan position indicators (CAPPIS) from 2- to 20-km height up to a distance of 150 km with a horizontal resolution of $2 \text{ km} \times 2 \text{ km}$ and 1-km vertical resolution.

b. Frequency of volume scans in the database

The great distances and inaccessible locations in the Amazon pose several difficulties in maintaining the SIPAM radar network that have a direct impact on the quality and frequency of stored data. Figure 2 shows the number of days per month with volumetric data stored for each GR for the period of operations. Note that the year 2008 has a low number of days with data stored basically in all the weather radars. The first five months of this year show only the MAO radar with information. The storage system was implemented at that time; hence the large number of gaps in the data stored.

The SGC radar also has data gaps in the months of November and December 2012. The same is true for the TFF radar in the months of October, November, and December 2009. The BVB radar has data gaps in five consecutive months in 2012. In MCP, there is a shortage of information between April and June 2012. Periods revealing problems of transmission and receipt of data can be identified in June 2010 and April 2012, where there are few data throughout the network.

In general, the radar presenting more data gaps is the PVH radar, while the CZS radar has one of the more complete series of the network. Missing data in Fig. 2 are due to transmission problems in the data, errors arising from mechanical breakdowns, and difficulty in transporting specialized technicians and spare parts. Possible sampling issues will be analyzed in the discussions.

c. Volume scan quality control

Among the factors that determine the quality of the extracted reflectivity data from weather radars is the

radar beam blocking (Westrick et al. 1999; Maddox et al. 2002; Lang et al. 2009) and the lack of proper calibration (Kitchen and Blackall 1992; Anagnostou et al. 2001). Several studies have been developed in the light of these problems and some of these methods are applied in the CAPPI's extraction process. For this study, the quality control is divided into two parts: mainly, the beam blockage based on topography effects and radar calibration.

1) TOPOGRAPHY

The evaluation of the topography is extremely important when using information from radar data, especially in complex topography regions. The radar beam blockage occurs mainly at low elevation angles and contaminates Z measurements because of signal losses or ground backscattering. These effects are further intensified when radar reflectivity factor is converted to rainfall R by known Z - R relationships that are used to estimate precipitation.

To verify the possible existence of topographical interference that can influence the precipitation estimates, we estimate the percentage of the blocked beam based on the partial beam blockage (PBB) method (Bech et al. 2003) adjusted with 90-m digital elevation model (DEM) data (U.S. Geological Survey; <http://www.geocomm.com>) maps. The beam geometry used in the PBB correction method is based on the equations of Doviak and Zrnić (1993).

From Fig. 3, the fraction of the blocked beam is seen as well as the simulation of the propagation of the energy beam for the first elevation (0.9°), plus the maximum integrated topography in azimuth and the maximum fraction of the blocked beam integrated in azimuth, for the SGC, STM, and BVB radars. Not included are the graphs for other radars, as they did not present significant interference with topography (see topography in Fig. 1). The PBB simulation for the SGC radar indicates a blocked fraction not exceeding 50% for the 0.9° elevation. The most significant values are seen in the northwest sector ($\sim 280^\circ$) and in northeastern quadrant (20° - 40°). The northwestern radar beam interference observed in Fig. 3a (left) is highlighted at Fig. 3a (right), which shows the incidence of the radar beam on the topography around 20-km and 300-m height. This orographic feature can be checked in the topographic map (Fig. 1). The northeast interference is associated with the incidence of the radar beam in the topography that is approximately 130 km from the radar, known as Pico da Neblina. Even a distant topographical feature as Pico da Neblina with 2972-m altitude (the highest elevation in Brazil) interferes with the radar beam propagation, with PBB up to 25%.

For the STM radar (Fig. 3b), the PBB simulations show topography blocking only in the southern radar sector, not exceeding 20%. In this case, the incidence of the beam on the surface is about 10 km from the radar and the topography causing the interference does not exceed 200 m in height.

For BVB (Fig. 3c), the PBB simulations show a few sectors with obstruction, and in the southeastern sector ($\sim 170^\circ$) the blocking is total. In this sector, the blocking is caused by topography near the radar, about 30 km away and ~ 1 km in height. The southwestern beam is associated with incidence on the topography at two positions: the first approximately at 210° and the second at 240° , having approximately 30% of the beam blocked.

The simulations were performed for a standard atmosphere and for superrefractive conditions (Bean and Dutton 1968). Because of the elevation settings for each radar, PBB interference for superrefractive conditions was similar to propagation situations in a standard atmosphere. Correction for this effect can be applied by computing the portion of beam blockage through radar viewing geometry and a detailed DEM (Andrieu et al. 1997). In this study, no attempt was made to correct this effect, and the sectors contaminated by partial beam blockage greater than 20% were flagged as uncertain.

Quality-controlled radar volume scan reflectivity data processed by the Ground Validation System (GVS) package developed by the TRMM office (Kulie et al. 1999) were used in this study. In short, GVS attempts to remove nonprecipitation echoes associated with returns by topography, insects, birds, second trips, physical structures, and anomalous propagation. The quality-control algorithm involved in the system was chosen by the TRMM Science Team and is a modified version of procedures developed by Rosenfeld et al. (1995). Sectors with more than 20% of the beam blocked were removed. The amount of data removed for this reason is less than 10% in all radars. A few minor interferences have been found near the radars because of vegetation, but these have been removed by the filter since they are found within the first 4 km with reflectivities between 12 and 20 dBZ.

2) CALIBRATION

Radar reflectivity data quality control is carried out in order to mitigate errors arising from operational faults and/or lack of proper calibration. Radar calibrations customize problems related to sensor electronics, antenna gain, and changes in the radome as well as in the transmitted power or high-powered vacuum tube (magnetron) lifetime losses.

Usually a known target is employed to evaluate the absolute radar calibration, that is, metallic spheres or corner reflectors (Scarchilli et al. 1995). However, the

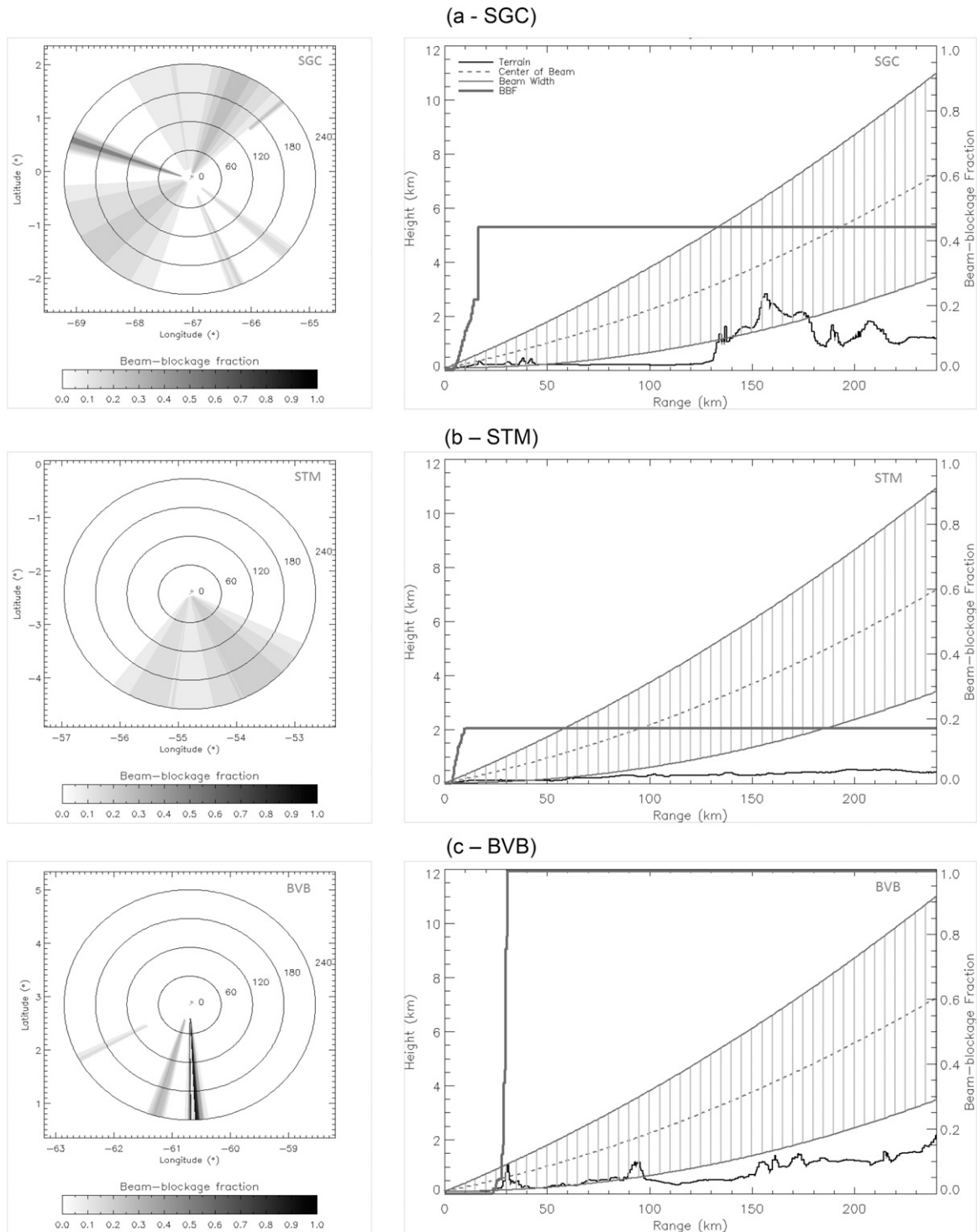


FIG. 3. (left) Examples of beam blockage fraction and (right) horizontal view simulation of beam propagation of a radar's first elevation angle as a function of range (km) from the radar. The fraction blocked is integrated in azimuth, and the maximum topography around the azimuth is indicated at the bottom. (a) SGC; (b) STM; (c) BVB.

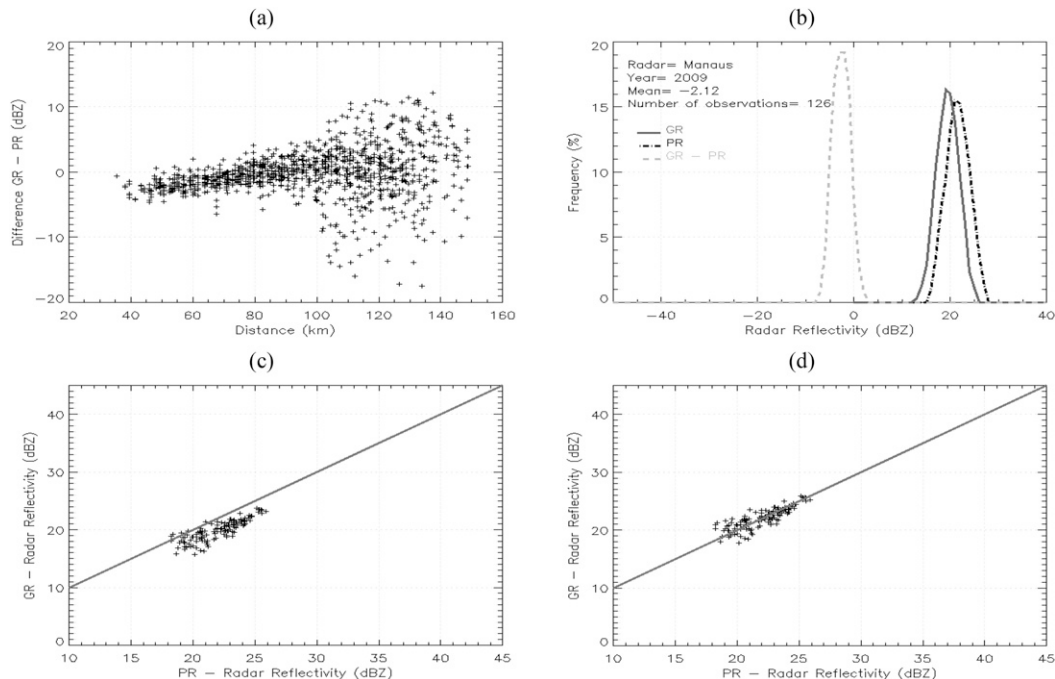


FIG. 4. Calibration of MAO GR reflectivity based on TRMM PR reflectivity for the year of 2009. (a) Difference in reflectivity between GR and PR as a function of distance from GR location. (b) Frequency distribution of reflectivity for the nonadjusted GR series, PR, and the difference between GR and PR. (c) Nonadjusted GR vs PR. (d) Adjusted GR as a function of PR.

SIPAM weather radar network presents logistical difficulties that inhibit this periodical procedure. To overcome this issue, we employed the methodology proposed by Anagnostou et al. (2001) that uses TRMM PR measurements as reference. Basically, this procedure intercompares coincident GR and TRMM PR radar reflectivity measurements. As GR and TRMM PR present different characteristics (frequency, antenna beamwidth, gate resolution, volume scan configuration, and location), it is important to define a common 3D grid box that provides a base for comparison. Differences were found between the GR and the TRMM PR for each year and each radar. The bias corrections were applied for each year individually, and these differences are defined for each radar.

For each radar, GR and TRMM PR, we define a three-dimensional base (3D CAPPi) centered on GR position, with horizontal resolution of 5×5 km and 2 km in the vertical. The resolution used follows the methodology developed by Anagnostou et al. (2001) that better evaluates the existence of bias at ground-based weather radars. Analyses of reflectivity fields (sections 4b, 4c, and 4d) use higher resolution in the construction of 3D CAPPis (section 3), which provides better quality in reflectivity information. Because of the GR beamwidth of 1.8° , the 3D CAPPis are limited to 10–60 km to

avoid elevation gaps of the shorter distances and beamfilling effects at further ranges, respectively. Furthermore, the 3D CAPPis are computed only for the levels of 7 and 15 km every 1 km to guarantee the presence of ice particles that fall over the Rayleigh scattering regime (Anagnostou et al. 2001; Anagnostou and Morales 2002). Moreover, to ensure compatible measurements between Ku- and S-band weather radars in the Rayleigh scattering regime, only TRMM PR profiles classified as stratiform and with radar reflectivity between 18 and 35 dBZ are used for the intercomparison.

We inspected the temporal evolution of the bias for each radar, and in order to illustrate this analysis, here we only show MAO weather radar (e.g., Fig. 4). Figure 4a shows matched radar reflectivity differences between GR and PR as a function of range, and it is possible to observe a bias in the MAO radar during 2009, in addition to the variability increase beyond 60–80 km from the radar that is caused by the large beamwidth of MAO radar. To find the mean GR radar reflectivity bias, we compare the values obtained for each radar with TRMM PR considering the whole 3D box with a maximum time difference of 3 min. Based on the matched measurements, we build radar reflectivity histograms that evaluate the behavior of the TRMM PR and GR probability density distribution for all SIPAM weather

TABLE 1. Calibration of the SIPAM radar network. The BIAS describes the difference in reflectivity decibels between the GR and the TRMM PR. Positive values should be subtracted from the GR reflectivity, negative values should be added. NCM indicates no case matches between the two sensors GR and TRMM PR. ORB indicates number of orbits used to compute the bias.

Radar	2008		2009		2010		2011		2012	
	ORB	BIAS	ORB	BIAS	ORB	BIAS	ORB	BIAS	ORB	BIAS
BEL		NCM	27	-1.0	25	3.9	23	-10.3	17	-6.8
STM	08	4.0	25	1.7	25	4.9	18	3.7	24	1.7
MAO	09	5.4	16	-2.1	15	-6.9	11	-5.9	17	-8.0
TFF	08	5.5	19	9.7	18	5.1	15	4.7	38	6.5
PVH	09	1.7	27	0.5	02	-1.0	11	5.3	25	5.9
CZS	05	10.3	39	8.3	18	7.8	23	9.6	24	8.3
TBT	12	6.2	33	-3.6	29	-0.3	30	0.3	29	-1.3
SGC		NCM	28	0.6	27	7.0	20	5.2	18	6.3
MCP		NCM	28	-9.7	18	-5.0	19	-5.6	33	-7.4
BVB	06		5.1	21	-1.9	13	-11.2	09	3.5	13

radars and for each year analyzed. As an example, Fig. 4b shows radar reflectivity factor histograms for 126 coincident measurements of MAO weather radar and TRMM PR, and the corresponding GR and TRMM PR difference for the year 2009 based on 16 TRMM orbits. Based on these distributions, it is possible to observe that MAO radar is underestimating the radar reflectivity measurements, and according to the histogram difference it reaches a value of -2.12 dBZ. Similarly, it is possible to observe matched GR against TRMM PR before and after calibration correction (Figs. 4c,d).

Table 1 shows the radar reflectivity factor bias for each SIPAM GR for each year and the number of TRMM orbits used. Among all the 10 weather radars, CZS presents the largest bias in all years that is essentially overestimating the measurements. In 2008, CZS GR had a reflectivity overestimation of 10.3 dBZ, while the BVB GR in 2010 and BEL in 2011 showed an underestimation of 11.2 and 10.3 dBZ, respectively. For the TBT GR, the bias was very small for 2010 and 2011, with bias between ± 0.3 dBZ, while in the other years it oscillated from 6.2 dBZ at 2008 to -3.6 dBZ for 2009. In 2009 no case matches (NCM) were found at SGC, MCP, and BEL mainly because of data gaps on those weather radars. Based on the biases evaluated on Table 1, GR CAPPIS were computed taking into account these corrections. In all cases, positive values should be subtracted from the GR reflectivity and negative values should be added. In NCM case, the bias of the following year is used for correction of the year. Thus the radar reflectivity values used in the following sections have been bias corrected.

3. Methodology

Five years of volumetric data of the SIPAM radar network (2008–12) are analyzed by focusing on the

rainiest season (WET), driest season (DRY), rainiest to driest transition season (TRA1), and driest to rainiest transition season (TRA2) of each region around each GR. The selection of WET and DRY for each region is based on the 21-yr rainfall climatology presented by Rao and Hada (1990) that is shown on Table 2. In most GR, WET occurs between the Southern Hemisphere summer solstice (December) and autumn equinox (March), except for BVB, which features the rainiest months in June–August. Similarly, the DRY in most GR occurs between the Southern Hemisphere winter solstice (June) and the spring equinox (September), again with the exception of BVB that occurs in January–March.

The corrected radar reflectivity fields Z (section 2c) analyses are based on 3D CAPPIS constructed by the method developed by Anagnostou and Krajewski (1997). The 3D boxes are limited to 150 km from the GR and from 2- to 20-km height. The 3D boxes have a horizontal resolution of $2 \text{ km} \times 2 \text{ km}$ and 1 km in the vertical. The climatological contoured frequency by altitude diagrams (CFADs) were constructed with 1-dBZ class intervals for every 1-km height between 2 and 14 km of height. Only pixels with surface radar reflectivity classified as “certain rain” (i.e., $Z \geq 10$ dBZ) are used.

Furthermore, radar reflectivity fields were also used to build daily cycles of frequency of occurrence for each month. The frequencies of occurrence of convective and stratiform fractions were selected from the 3-km level, based on Steiner et al. (1995) methodology. Because of the beamwidth (1.8°), gate resolution (500 km), and elevation strategy, good sampling is achieved at 150-km radar for CAPPIS above 3 km. At lower heights the coverage is restricted to 100–120 km. Moreover, both sidelobe and ground clutter contaminations are absent at or above 3 km. Finally, it is important to state that the

TABLE 2. Definition of the rainiest trimester (WET), the driest trimester (DRY), months between rainiest and driest (TRA1), and months between driest and rainiest (TRA2) for the area of each of the SIPAM radars, based on Rao and Hada (1990).

Radar	WET season	TRA1 season	DRY season	TRA2 season
BEL	Feb–Apr	May–Jul	Aug–Oct	Nov–Jan
STM	Feb–Apr	May–Jul	Aug–Oct	Nov–Jan
MAO	Feb–Apr	May–Jun	Jul–Sep	Oct–Jan
TFF	Mar–May	Jun	Jul–Sep	Oct–Feb
PVH	Dec–Feb	Mar–May	Jun–Aug	Sep–Nov
CZS	Feb–Apr	May	Jun–Aug	Sep–Jan
TBT	Jan–Mar	Apr–May	Jun–Aug	Sep–Dec
SGC	Apr–Jun	Jul	Aug–Oct	Nov–Mar
MCP	Feb–Apr	May–Aug	Sep–Nov	Dec–Jan
BVB	Jun–Aug	Sep–Dec	Jan–Mar	Apr–May

0°C isotherm is above 4.5 km, so using 3 km there is no contamination from the bright band. For the frequency diagrams, rain and no-rain pixels were considered, resulting in the unconditional frequency. Therefore, the rain fraction totals (convective plus stratiform) will have a maximum frequency of 11%.

4. Regional variability in the Amazon

This section presents the results on rainfall variability as seen by the SIPAM radar network. Initially the variability based on lightning data is presented, followed by the analysis of the radar reflectivity for each region. The annual and diurnal cycle of reflectivity and frequency distribution as a function of altitude are presented in the subsections.

a. Regional variability of lightning

The annual cycle of the frequency of lightning detected by the STARNET network, within the 150-km range of each GR for the period 2008–12 is shown in Fig. 5. It is interesting to note the annual cycle similarity among SGC, TBT, TFF, MAO, CZS, and PVH radar areas, with the lightning activity starting between June and July and reaching a peak around September and October. Another feature observed is the well-distributed lightning occurrence throughout the year for the MCP and STM regions, which do not have well-defined seasonal peaks.

Note that in six of the areas around the SIPAM GR, the highest frequencies of lightning occurred in the months of transition between DRY and WET (MAO, TBT, TFF, CZS, PVH, and STM), while for three radars the highest frequencies of lightning occurred in the transition between WET and DRY (BVB, BEL, and MCP), and for only one radar did the highest frequencies of lightning occur in the DRY months (SGC).

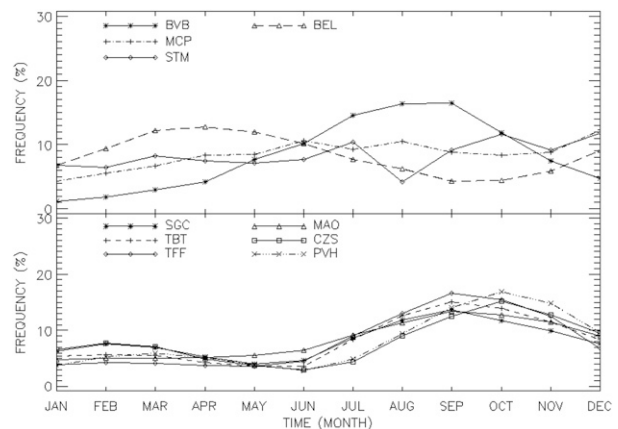


FIG. 5. Monthly relative frequencies of lightning strokes in a 150-km area around each weather radar. The frequencies are obtained from the STARNET for the period of 2008–12.

According to Saraiva (2010) during the transition between DRY to WET, the observed systems at MAO GR were deeper and with greater convective activity as well as higher occurrence of lightning. Albrecht et al. (2011) also found that most of the lightning activity was observed in southwestern Amazonia, close to the PVH GR, in the transition period between dry and wet seasons. Those studies indicate that the gradual increase of water vapor in the atmosphere and the existence of convective inhibition were the main processes related to the formation of rain clouds, while a secondary process could be attributed to the enhanced concentration of aerosol associated with biomass burning. The enhanced aerosol concentration provided by biomass burning inhibits the warm-rain processes in the Amazon basin and enhances ice production, which in turn helps the development of deeper convective clouds (Andreae et al. 2004).

b. Annual and diurnal cycle

The annual and diurnal cycle are based on the convective (CV) and stratiform (ST) fraction at 3-km height obtained according to the method of Steiner et al. (1995) and are shown in Fig. 6. The cycles are binned monthly and hourly for the relative frequency of occurrence of Z. The Amazon climate includes a combination of several factors that influence the precipitation regimes, as discussed in previous sections. In this sense, in the coastal region of the Amazon, which comprises the BEL radar (Fig. 6a), rainfall is distributed throughout the year and has a total average of around 2500 mm yr⁻¹ (Figueroa and Nobre 1990). In this region, the precipitation usually occurs in the afternoon because of the formation of squall lines triggered by moisture convergence associated with the sea breeze (Cohen et al. 1995; Alcántara

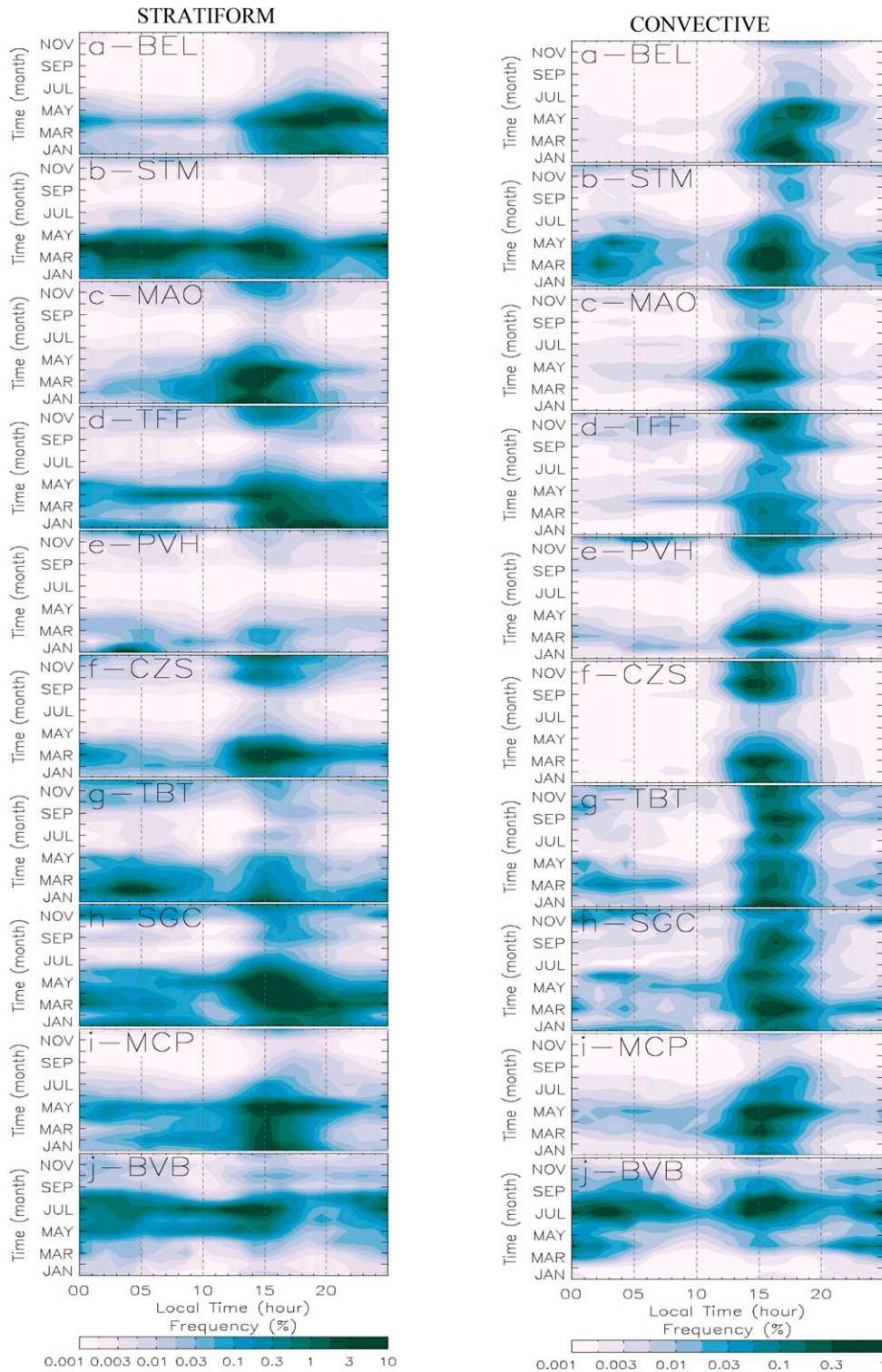


FIG. 6. Annual and diurnal cycles by binned monthly and hourly relative frequency of occurrence of (left) stratiform and (right) convective fractions for the SIPAM radars: (a) BEL; (b) STM; (c) MAO; (d) TFF; (e) PVH; (f) CZS; (g) TBT; (h) SGC; (i) MCP; (j) BVB. Vertical dashed lines correspond to local time, every 5 h.

et al. 2011). In the case of BEL-ST, the highest frequency of stratiform fraction occurs between 1400 and 2200 local time (LT; $\sim 10\%$ in April, 1700 LT), especially between the months of April and May. The BEL-CV is more frequent during the afternoon, between 1200 and 1700 LT and extends from the month of January to June (peak occurs in February, between 1500 and 1600 LT, $\sim 1\%$).

The central region of the Amazon may be associated with the area covered by the STM, MAO, and TFF weather radars. The STM (Fig. 6b) is noted by a ST fraction well distributed throughout the day during the months of February to April, while the CV fraction presents two peaks of occurrence, one in the afternoon (1300–1600 LT; peak occurs in March, between 1400 and 1500 LT, $\sim 1\%$) and one between night and dawn ($\sim 0.2\%$ in March, 0200 LT, and in May, 0300 LT). Studies show that this region is influenced by the river-breeze circulation imposed by the Tapajós River (Cohen et al. 2014; Silva Dias et al. 2004) and also by the passage of squall lines moving from the northern coast to the central Amazon (Cohen et al. 1995). As a possible result of the squall lines, a pronounced peak is seen in the ST fraction between night, dawn, and early morning. Possibly the peak frequency well marked in the afternoon is associated with local convective activity (Cohen et al. 2014). Nonetheless, a few of the squall lines originating at the northern coast propagate several hundreds of kilometers inland (Cohen et al. 1995), and while crossing STM in the evening and early night they are already losing intensity. In the following day, however, sunlight/solar radiation enhances convection and allows further propagation.

Precipitation in the MAO radar region (Fig. 6c) is influenced by the passage of squall lines, river-breeze convective activity imposed by the Rio Negro (De Oliveira and Fitzjarrald 1993; Dos Santos et al. 2014), and local convective systems (Oliveira 1986; Satyamurty et al. 1998). In MAO-ST, the major events are observed between 1100 and 1500 LT (peak $\sim 10\%$; in March, 1300 LT; in April, 1400 LT) both in the rainy season (February–April) and at the transition between wet and dry seasons (May–June) and between dry and wet seasons (December–January); however, the CV peak fraction is found in the wet season (April) and with less intensity ($\sim 0.6\%$) it extends to the dry season (July–September) and up to the dry–wet transition season (October–January) although it is less frequent ($\sim 0.1\%$) and focused primarily between the end of morning to midafternoon. Saraiva (2010) analyzed the behavior of precipitation systems in the region covered by the MAO radar and found that in the dry and dry–wet transition season, the precipitation systems were more developed

vertically and had the same area and volume as in other seasons; however, they had higher rainfall volumes and also had a higher incidence of lightning.

In the TFF region (Fig. 6d), as well as in MAO, rainfall is due to the factors described above. Less frequently, the squall lines originating at the northern coast reach the TFF region. There are no studies that describe this region, and the main conceptual models are taken from the daily weather forecast operations. Frequencies of rainfall observed in the TFF-ST throughout the night and early morning are probably due to the passage of weakening squall lines that contribute light rain and overcast skies (Negri et al. 2002; Nesbitt and Zipser 2003; Rickenbach 2004). The highest frequencies observed in TFF-ST are throughout the afternoon and early evening, in the months of the wet season and wet–dry transition season (maximum $\sim 5\%$). The convective fraction has a higher frequency of occurrence in the dry–wet transition season (peak $\sim 1\%$ in November, 1400 LT).

In the southern Amazon, comprising the area of CZS and PVH weather radars, rainfall is influenced by frontal systems that interact and organize the local convection (Satyamurty et al. 1998; Longo et al. 2004), especially in the Southern Hemisphere summer. The annual cycle seen in Fig. 6 indicates that for CZS and PVH a well-defined dry season is established between the months of June and August. However, even though rainfall is infrequent, the CZS-CV has frequencies in less rainy months of this region, indicating the presence of precipitating active systems, which are possibly related the Andes Mountain range (Vera et al. 2006). Also in the CZS-CV, there are frequent peaks in March ($\sim 1\%$; rainy season in the region) and October ($\sim 0.8\%$; dry–wet transition season), between 1300 and 1500 LT, while in PVH-CV there is only one peak in March ($\sim 0.8\%$). PVH and CZS show a remarkable discontinuity during June and July possibly caused by cold wind incursions associated with the penetration of frontal systems that stabilize the atmosphere in the southern Amazon region (Parmenter 1976; Hamilton and Tarifa 1978; Marengo et al. 1997).

In western Amazon region, in the area comprising TBT radar (Fig. 6g), the weather is affected by factors characteristic of both the northwest region (low-level flow forced by the Andes) and the southwest region (organization of convection by frontal systems; Satyamurty et al. 1998). The accumulated annual rainfall reaches around 2800 mm yr^{-1} (Figuerola and Nobre 1990). The ST portion is evenly distributed throughout the day, between the months of January and May, with a peak between 0100 and 0800 LT (peak $\sim 10\%$) and a peak between 1400 and 1600 LT (peak $\sim 10\%$). The convective fraction is well

distributed throughout the year, between 1400 and 1900 LT.

In the northwest region of the Amazon, the area surrounding SGC (Fig. 6h), we find a record of approximately 3500 mm yr^{-1} (Figueroa and Nobre 1990). In this region it is not possible to define a dry season; there is just a less-rainy season (August), as seen in SGC-ST and SGC-CV. The ST portion is distributed throughout the year and the higher frequencies are seen between the months of November and May, with peaks between the afternoon and early evening (between 1200 and 1800 LT; $\sim 10\%$). The CV portion also shows uniform annual distribution and occurs between 1200 and 1700 LT (peak in March between 1400 and 1500 LT; $\sim 1\%$). In this region, the trade winds associated with the ITCZ favor the rainfall accumulation. The water vapor undergoes the orographic uplift at the Andes, producing clouds and rainfall (Figueroa and Nobre 1990; Vera et al. 2006).

Finally, the regions around the BVB and MCP radars are basically affected by the displacement of the ITCZ (Satyamurty et al. 1998). In BVB, the predominance of CV and ST fraction occurs between May and August. ST fraction has a pronounced peak along the morning to early afternoon ($\sim 10\%$ in July, 1300 LT), while the CV portion presents two peaks: one in the night (2200–0300 LT; $\sim 1\%$ in July, 0300 LT) and the other in the early afternoon (1200–1500 LT; $\sim 1\%$ in August, between 1400 and 1500 LT). In MCP, the CV fraction has only one peak and it is concentrated in the afternoon (1200–1600 LT $\sim 1\%$ in May, 1500 LT) and is most common between February and May. The ST fraction follows the CV fraction and has a single peak frequency, also concentrated in the afternoon, especially between January and May ($\sim 1\%$ in May, 1500 LT).

c. Regional variability of radar reflectivity fields— Frequency distribution as a function of altitude

The three-dimensional relative frequency distributions for radar reflectivity, as defined by Yuter and Houze (1995), synthesize the frequency distribution changes from low to high levels. The ordinate axis of the CFAD is height, while the abscissa is the radar reflectivity factor. The CFAD contours represent the frequency of occurrence of reflectivity at each vertical level. Here the CFADs are truncated at 14 km (below tropopause in the tropics) to eliminate the noise effects due to few samples at higher levels ($\leq 1\%$ of the total). Figure 7 shows the CFADs representing the average vertical structure of precipitation for each radar during the WET, DRY, TRA1, and TRA2 regimes. Since the TRA1 and TRA2 periods have fewer months, the statistics may not be as representative as for DRY and WET and may require further study.

The width of the reflectivity distributions with height is associated with the formation mechanisms of hydrometeors or type. Unimodal distribution at a given height implies the predominance of one process or one type of hydrometeor, while bimodal, multimodal, or broader distributions indicate the formation of several hydrometeors (Yuter and Houze 1995). The change in slope with the frequency and height can indicate an increase or decrease in precipitation, or even the presence of ice above the isotherm 0°C . According to Zeng et al. (2001) and Rowe and Houze (2014), as solid ice particles have lower refractive index than water (0.197 vs 0.93), the radar reflectivity can decrease as low as 6.7 dBZ when compared with water droplets. Therefore, a sudden decrease above the 0°C isotherm means the presence of ice crystals. The snow melting defines the occurrence of a bright band as the snowflakes are coated by water. As indicated by these authors, the following hydrometeors classification based on the Z measurements is established:

- Just above the 0°C isotherm—dry snow: $12 < Z < 32$ dBZ.
- At 0°C isotherm and just below—wet snow: $32 < Z < 42$ dBZ.
- From the surface up to 5-km height—rain: $Z > 30$ dBZ.
- Between 5- and 8-km height—graupel/hail, ice crystals, and supercooled water droplets: $25 < Z < 30$ dBZ.
- Above 8 km—ice crystals/dendrites: $Z < 15$ dBZ; aggregates: $15 < Z < 20$ dBZ.

As discussed earlier and shown by several authors, each of the Amazon regions is influenced by different precipitation mechanisms that may be associated with the different profiles seen in the CFADs. In BEL for example, the CFADs (Fig. 7a) have a width at low levels ranging from 10 to 40 dBZ featuring an unimodal distribution. Also in BEL, a bright band can be seen during most seasons (WET, TRA1, and TRA2) as indicated by an increased reflectivity (~ 1.5 dBZ) between 2 and 4 km, which is constant between 4 and 5 km; there is a sharp drop in reflectivity above this level. This is possibly due to the structure of the squall lines that have a leading edge with heavy rain and large portions of trailing stratiform rain (Cohen et al. (1995). High reflectivity values are identified in all seasons between levels 2 and 4 km (~ 28 dBZ), suggesting heavy rainfall throughout the year.

The diurnal cycle of stratiform fraction for the STM region shown in Fig. 6b indicates significant frequencies of occurrence throughout the day in the rainy season. This stratiform rain is observed in STM CFADs (Fig. 7b)

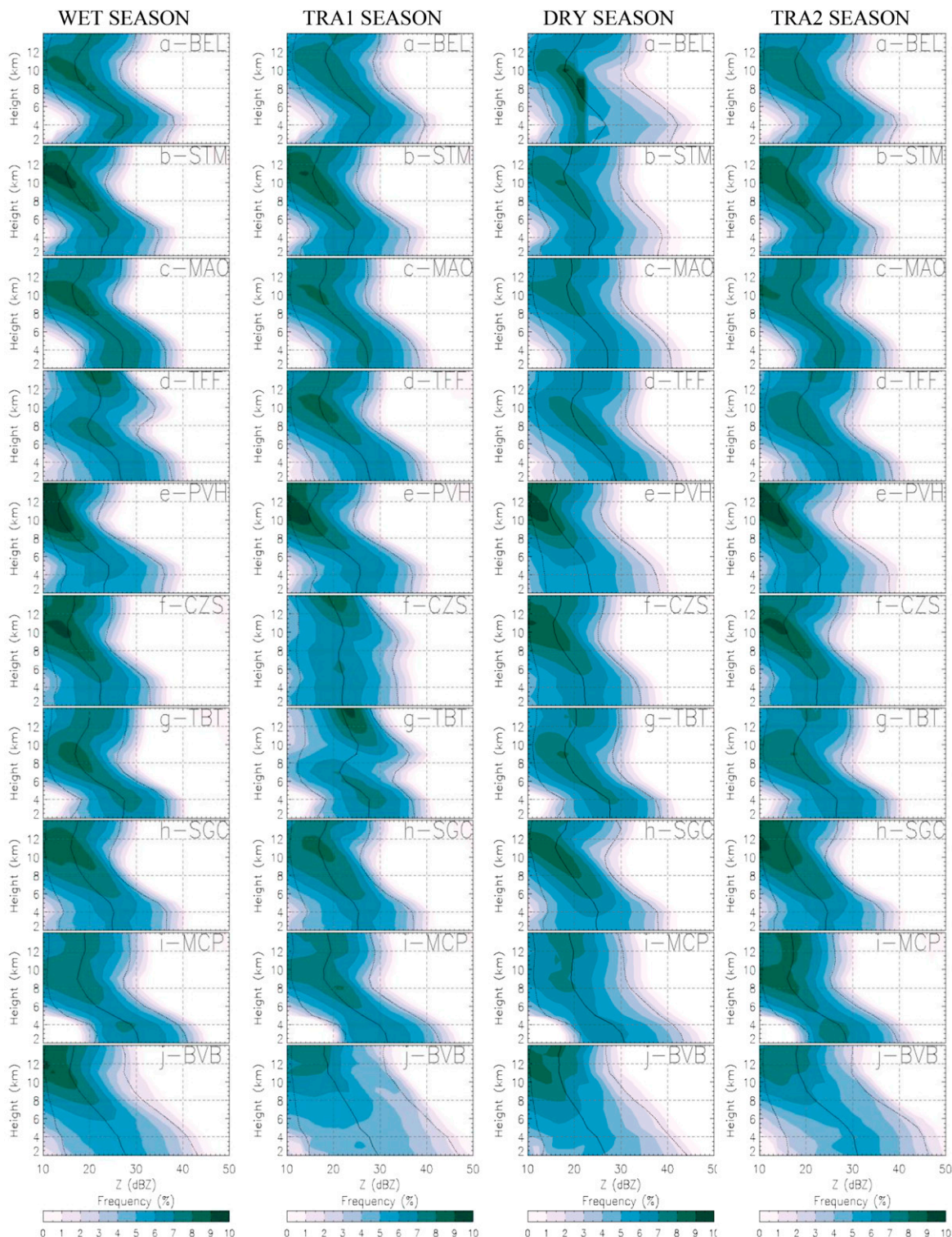


FIG. 7. Climatological CFADs of radar reflectivity for the 3D CAPPI collected in (left) WET, (center left) TRA1, (center right) DRY, and (right) TRA2 seasons for the SIPAM radars. CFAD bin size is 1 dBZ. The contours are at intervals of 1% of data per reflectivity decibel per kilometer, starting with the 1% $\text{dBZ}^{-1} \text{km}^{-1}$ contour. (a) BEL; (b) STM; (c) MAO; (d) TFF; (e) PVH; (f) CZS; (g) TBT; (h) SGC; (i) MCP; (j) BVB. Solid lines represent the median, and the dotted lines correspond to the 10th- and 90th-percentile boundaries of the distribution. Horizontal dashed lines correspond to height, every 4 km. Vertical dashed lines correspond to reflectivity, every 10 dBZ.

because of the presence of brightband features. During all seasons (WET, DRY, TRA1, and TRA2), the reflectivity values tend to increase around 2 to 4 km (~ 0.5 to 1 dBZ), remain constant between 4 and 5 km, and diminish above. In STM, the frequency of occurrence of lightning has no preferential period and remained approximately constant at 10% throughout the year. This fact is consistent with the presence of a well-defined melting layer in all CFADs this region.

Unlike the CFADs in BEL and STM, the CFADs in MAO (Fig. 7c) do not show an increase of reflectivity between 2 and 4 km but show approximately constant values in this layer. According to Steiner et al. (1995), stratiform profiles are associated with increased reflectivity between the surface and the melting layer or constant reflectivity values between these layers. The profiles are consistent with Fig. 6c, showing significant amounts of stratiform rain fractions between the rainy periods and wet-dry transition. Moreover, another important feature of the stratiform precipitation is CFADs with large widths between the lowest and the highest value of reflectivity in these levels. In MAO, the widths range from between 16 and 40 dBZ in WET, 16 and 42 dBZ in TRA1, 14 and 45 dBZ in DRY, and 15 and 41 dBZ in TRA2. Between 4 and 8 km, the gradient of reflectivity in DRY (~ 1.6 dBZ km⁻¹) and TRA1 (~ 1.8 dBZ km⁻¹) seasons are slightly smaller than in WET (~ 2.0 dBZ km⁻¹) and TRA2 (~ 1.9 dBZ km⁻¹). Above 8 km, median values are high and the high frequencies are lower than 15 dBZ in TRA2, suggesting dendrites, between ~ 15 and 20 dBZ in TRA1 suggesting aggregates, and between ~ 10 and 20 dBZ in WET and DRY, suggesting the formation of more than one type of ice crystal and/or larger ice particles.

As with MAO, the region of TFF radar presents the same weather systems that favor the production of rainfall. The TFF radar CFADs (Fig. 7d) have a median distribution at 2 km in which high reflectivity values are observed, with the median at 27 dBZ in WET and TRA2, 28 dBZ in TRA1, and 29 in DRY. These are approximately 2–3 dBZ larger than values seen in the CFADs of BEL, STM, and MAO. The widths of CFADs at 2 km show values ranging between 10 and 41 dBZ in WET, 11 and 43 dBZ in TRA1, 11 and 47 dBZ in DRY, and 11 and 43 dBZ in TRA2. Between 4 and 8 km, TRA1 and TRA2 profiles show gradients of 1.9 and 1.7 dBZ km⁻¹ in WET and DRY. Above 8 km, the frequencies are more elongated vertically, unlike what is observed in MAO in the TRA1 season, suggesting only ice crystals of the aggregate type, which usually are between 15 and 20 dBZ at this height.

According to the annual and diurnal cycles of radar reflectivity of PVH and CZS radars, there is similarity

between the frequencies (Fig. 6); however, CFADs show differences. In PVH the CFADs (Fig. 7e) show convective features in the WET, TRA1, and TRA2 seasons, with radar reflectivity increasing up to the level of 4 km and a well-defined melting layer. In the DRY season, no bright band is defined and the mean profile decreases with height, at 2 to ~ 10 km. Above 8 km there are the highest frequencies of occurrence of all radars ranging between 10 and ~ 15 dBZ and suggesting large amounts of ice crystals of the dendrite type at high levels.

In CZS the CFADs in the WET, TRA1, and TRA2 seasons are approximately constant between 2 and 4 km. In the DRY season it is similar to the DRY season seen in the PVH CFAD, with a decrease with height. The widths of CFADs at 2 km show values greater in PVH (~ 10 –40 dBZ in WET, ~ 10 –41 dBZ in TRA1, ~ 10 –43 dBZ in DRY, and ~ 10 –42 dBZ in TRA2) than CZS (~ 10 –39 dBZ in DRY and 10–38 dBZ in other seasons), in all seasons, suggesting larger rainfall volumes. The high reflectivity values observed above the mixed layer in PVH have also been identified by Albrecht and Silva Dias (2005) and are consistent with the results reported by Petersen et al. (2002) that suggested a more robust mixed phase and more lightning in easterly wind regimes. In westerly wind regimes, however, driven by the presence of the SACZ, the radar reflectivity vertical profile distributions showed a poorly developed bright band and lower reflectivity at low levels.

Median values of TBT CFADs (Fig. 7g) at low levels show higher values than in SGC, about 2 dBZ. However, between 4 and 8 km, the gradient is more significant, ranging from ~ 2.5 dBZ km⁻¹ in WET, to ~ 2.2 dBZ km⁻¹ in DRY and TRA2, and to ~ 1.4 dBZ km⁻¹ in TRA1. Above 8 km, the radar reflectivity values tend to increase with height, except in TRA1. Higher frequencies are noted in the approximately 15–20 dBZ in WET and DRY and 10–20 dBZ in TRA2. The SGC radar differs from others by presenting the largest total annual rainfall of the entire Brazilian Amazon. The median distribution of SGC CFADs (Fig. 7h) shows almost constant reflectivity up to 4 km in height, and a small gradient (~ 0.5 dBZ km⁻¹ in all seasons) between 4 and 5 km high (around the mixing layer) and between 4 and 8 km (~ 1.7 dBZ km⁻¹ in WET, ~ 1.6 dBZ km⁻¹ in TRA2, ~ 1.5 dBZ km⁻¹ in TRA1, and ~ 1.4 dBZ km⁻¹ in DRY), also suggesting the presence of larger ice. Above 8 km, the higher frequencies have a greater range between 10 and 20 dBZ in WET, DRY, and TRA2, suggesting the formation of more than one type of ice crystal, and between 15 and 20 dBZ in TRA1. According to the annual and diurnal cycles, the rain is constant throughout the year in this region, and the peak of stratiform fraction occurs in the WET season, which justifies constant

TABLE 3. Summary of the main characteristics of CFADs and lightning in terms of dBZ height derivative (dBZ km^{-1}) for two layers, intensity of the median distribution (dBZ) at 2 and 4 km, and season of maximum lightning frequency. TRA1 means the transition from wet and dry season, while TRA2 from dry and wet season.

Radar	2–4 km				4–8 km				2 km				4 km				Season max lightning
	WET	TRA1	DRY	TRA2	WET	TRA1	DRY	TRA2	WET	TRA1	DRY	TRA2	WET	TRA1	DRY	TRA2	
BEL	1.6	1.4	1.4	1.5	-1.9	-1.5	-1.5	-1.9	24	25	24	25	27	28	27	28	WET
STM	0.8	0.6	0.6	0.7	-1.5	-1.5	-1.0	-1.4	22	23	23	22	24	24	24	24	DRY
MAO	0.1	-0.2	-0.1	0.1	-2.0	-1.8	-1.6	-1.9	27	27	27	26	27	27	27	26	DRY
TFF	-0.3	-0.5	-0.6	-0.4	-1.7	-1.9	-1.7	-1.9	27	28	29	27	26	27	28	27	DRY
PVH	0.5	0.4	-0.4	0.2	-1.7	-1.8	-1.2	-1.2	23	25	24	23	24	26	23	23	TRA2
CZS	0.1	0.1	-0.2	0.1	-1.3	-0.2	-1.1	-1.1	22	22	22	22	22	22	22	23	TRA2
TBT	0.1	0.1	-0.1	0.1	-2.5	-1.4	-2.2	-2.2	27	28	28	26	27	28	27	27	TRA2
SGC	0.2	0.1	0.1	0.2	-1.7	-1.5	-1.4	-1.6	25	25	25	24	25	25	25	25	DRY
MCP	-0.8	-1.0	-1.2	-0.9	-2.6	-2.6	-2.1	-2.6	31	32	31	29	29	30	28	27	TRA1
BVB	-0.8	-1.0	-0.9	-0.4	-1.7	-1.3	-1.4	-2.1	28	30	27	31	26	28	25	30	WET

values of reflectivity at low levels and high inclination after the mixing layer.

According to Liu et al. (2008), continental (ocean) systems are more (less) intense, with higher (lower) value of maximum reflectivity. Below the melting level, increases in reflectivity toward the surface are seen in oceanic CFADs but they remain almost vertical on land CFADs. In this sense, we can associate these with the MCP radar CFADs (Fig. 7i), for which in all periods there is a decrease in reflectivity with height, ranging from $\sim 1 \text{ dBZ km}^{-1}$ between 2 and 4 km and $\sim 2.5 \text{ dBZ km}^{-1}$ between 4 and 8 km. The CFADs of all seasons are very similar and do not represent a classic mixed layer, suggesting smaller ice particles and weaker upward movements than in other regions of the Amazon. This justifies the low frequency of occurrence values of lightning throughout the year in this region (Fig. 5). This fact is associated with the proximity of Atlantic Ocean ($\sim 160 \text{ km}$), justifying features of CFADs typical of oceanic systems, as observed by Liu et al. (2008).

The ITCZ seasonally migrates from its position farther north ($\sim 14^\circ \text{N}$) during August–September, to its position farther south ($\sim 2^\circ \text{S}$) during March–April. This seasonal migration of the ITCZ plays an important role in determining the rainy season BVB region (Satyamurty et al. 1998). Outside this period, rainfall can be associated with local convection and favored by the local topography (see Fig. 1). This may be one of the hypotheses for the CFADs of BVB (Fig. 7j) to present great variability at low levels (2 km), with values ranging from 10 to 47 dBZ in WET, 10 to 50 dBZ in TRA1, 10 to 47 dBZ in DRY, and 14 to 50 dBZ in TRA2. This large variability continues from 4 to 8 km and extends above 8 km. The slope of the median distribution between 4 and 8 km follows the same pattern in all seasons: $\sim 2.1 \text{ dBZ km}^{-1}$ in TRA2, $\sim 1.7 \text{ dBZ km}^{-1}$ in WET, and

$\sim 1.4 \text{ dBZ km}^{-1}$ in TRA1 and DRY. Above 8 km there is greater reflectivity frequency of occurrence ($\sim 8\%$) around 10–15 dBZ, suggesting ice crystals of the dendrite type. Another reason the BVB CFADs might differ from other distributions would be that the corrections imposed on the radar reflectivity fields did not completely remove contamination associated with beam blocking (e.g., trees and building sites).

The precipitation characteristics under the influence of different wind regimes in the region of the 10 radars should be examined in a subsequent article.

d. Overview

The climatological CFADs indicate great variability in precipitation structure for the 10 radars analyzed, confirming that each region has its own variability in relation to precipitation (Figueroa and Nobre 1990), possibly as a function of the different acting weather systems (Molion 1987; Satyamurty et al. 1998). The annual and diurnal cycle of the reflectivity fields and frequency of lightning confirmed this. Table 3 summarizes some important aspects of the CFADs and lightning. Regarding CFADs, the summary includes median gradients between 2 and 4 km and 4 and 8 km, as well as the intensity of radar reflectivity in the 2- and 4-km levels. In the lightning summary, the seasons with the highest frequencies are indicated. When this maximum occurs from the wet to dry transition season, this is indicated as TRA1, and when it occurs from the dry to wet transition, it is indicated as TRA2.

When the gradient of CFADs show negative (positive) values, a decrease (increase) of the reflectivity occurs with height. Positive values around 4 km suggest the presence of a bright band, and positive values between 2- and 4-km height might indicate the presence of evaporation found on deeper clouds. In general, the regions with bright band in all seasons were the BEL,

STM, and SGC. On MAO this is found during the WET and TRA2 seasons. In the southwest and western Amazonia (PVH, CZS, and TBT), the bright band is noted during WET, TRA1, and TRA2 seasons. However, in all seasons of the year there is no bright band defined in TFF, MCP, and BVB radar. Profiles from 4 to 8 km with changes in slope with height, indicating a decrease, were observed in all radars and were more intense in MCP (~ -2.1 dBZ km⁻¹ in the DRY season and ~ -2.6 dBZ km⁻¹ in others seasons). In MAO (~ -2.0 dBZ km⁻¹) and TBT (~ -2.5 dBZ km⁻¹) intense values were noted in the WET season. Higher median profiles at the 2-km level were identified in MCP (~ 31 dBZ) and BVB (~ 28 dBZ), while lower values are identified in CZS (22 dBZ at all stations) and STM (~ 23 dBZ).

The BVB and MCP radars do not show a well-defined melting layer, and all median profiles decrease with height or they increase as the precipitating particles fall. This effect is characteristic of a coalescence process and might explain why the distributions are broader close to the surface, compatible with oceanic tropical systems (Petersen and Rutledge 2001; Liu et al. 2008). However, in BEL, which is even closer to the Atlantic Ocean (~ 150 km), the mean profiles show the evaporation process below 4-km height and accretion/aggregation aloft. This suggests that in the rainy season there are strong updrafts and downdrafts. These BEL features show a combination of oceanic and continental systems characteristic of coastal regions (Petersen and Rutledge 2001). Note that only in these regions is the lightning activity more frequent during the WET season (BVB and BEL) and TRA1 (MCP) period where the ITCZ is acting over these regions. In MAO and STM this feature appears during the DRY season, the systems are more vertically developed, with higher production of ice particles responsible for the formation of lightning in the region. In TFF the lightning is more frequent in the DRY season, and a bright band is not observed in any season, but high reflectivity values between 2 and 4 km suggest an enhanced coalescence process and heavier precipitation. Machado et al. (1998) and Mohr et al. (1999) show that in the central Amazon (STM, MAO, and TFF), especially during the WET season, precipitation is often affected by MCSs of large proportions that cause intense convective rain, followed by large regions of stratiform precipitation. In SGC (northwestern Amazon), the precipitation is constant throughout the year and the CFADs are very similar in all seasons; however, the DRY season stands out because of a higher occurrence of lightning ($\sim 10\%$ higher than WET and TRA2 seasons; Fig. 5). The same may be seen in TBT (Fig. 6g), but the maximum of lightning occurs in TRA2.

In PVH and CZS, the systems also show the features observed in MAO radars (TFF, STM, TBT, and SGC) during the WET season. During the DRY season, the atmospheric stability (Satyamurty et al. 1998) inhibits the formation of precipitation systems (see CFAD PVH-DRY in Fig. 7e) and also the annual and diurnal cycle of reflectivity (Fig. 6e). However, the low relative humidity and the consequent increase in biomass burning activities are associated with the production of numerous particles that may be associated with intense precipitation systems and lightning during the TRA2 (Artaxo et al. 2002; Martins et al. 2009) or the easterly flow and high cloud base (Albrecht et al. 2011).

In general, during the DRY and TRA2 seasons, the systems are deeper, with more convective features including higher frequency of lightning; however, in the BEL, MCP, and BVB areas, intense precipitation systems are seen in WET with greater frequency of lightning.

5. Conclusions

This paper presents an analysis of the SIPAM weather radar network data in the Amazon by showing that there are marked differences and a few similarities between the various regions in terms of convective depth and intensity as well as in the annual and diurnal cycles of convective and stratiform fractions. Although several features are consistent with previous studies, this is the first time they have been addressed with data from an S-band weather radar network, rendering more information and details on the convection features in the Amazon as well as uncovering new features.

The present study has uncovered differences in behavior of Amazon rain clouds that are quite new. Raining systems in MCP and BVB have oceanic characteristics, while systems in BEL seem to be sometimes more oceanic and other times continental. Nocturnal peaks are found in many regions, both in stratiform fraction (CZS, PVH, TBT, SGC, BVB, MCP, TFF, STM, and BEL) and convective fraction (TBT, SGC, BVB, and STM). Similarities between the annual and diurnal cycles were also found in SGC (northwestern Amazon) and TBT (western Amazon), possibly because these two regions are near the Andes, although the TBT region is occasionally influenced by cold-air incursions (Satyamurty et al. 1998) from frontal systems, and the SGC region is occasionally influenced by moisture flow from the ITCZ (Figueroa and Nobre 1990; Vera et al. 2006).

Similar conditions with respect to radar reflectivity statistics are seen in some radars, possibly because the regions are affected by similar weather systems or are in similar geographical settings. Both CZS and PVH are

influenced by SACZ (Satyamurty et al. 1998), the topographical influence is similar for SGC and TBT (Figueroa and Nobre 1990; Vera et al. 2006), and BEL and STM are under the influence of the systems triggered by the sea breeze on the northern coast (Cohen et al. 1995; Silva Dias et al. 2004; Cohen et al. 2014). In MAO, TFF, and STM the systems are more vertically developed in the DRY season, while in BEL they are more vertically developed in the WET season. The intensity of the rain clouds and the higher frequency of lightning activity happen in different times of the year for the different regions. In some regions this takes place in the dry season (STM, MAO, TFF, and SGC), and in other regions this takes place in the transition from the dry to wet (PVH, CZS, and TBT) or wet to dry (MCP) seasons, while in others it is observed in the rainy season (BEL and BVB).

The variability found between the precipitating systems during the WET, DRY, TRA1, and TRA2 seasons is similar to the differences found in previous studies (e.g., Herdies et al. 2002; Rickenbach et al. 2002; Carvalho et al. 2002; Cifelli et al. 2002). Basically, the DRY season presents the majority of the convective profiles in most regions, similar to an easterly wind regime. Peculiar characteristics for each region are analyzed and need to be investigated separately, namely, the influence of the different weather systems as well as different wind regimes defined by the larger-scale circulation. Convective processes and the formation of precipitation systems are associated with physical aspects of large-scale, mesoscale, microphysical, and local (topography and vegetation) features. The effect of the weather systems is seen in the annual and diurnal cycle of the radar reflectivity fields. Issues related to these peculiarities must be taken into account for future research and raise other questions as well: Is there intraseasonal variability of precipitation systems, and is there an associated wind regime for each region similar to the one seen in the southwest Amazon? Could this variability be associated with the zonal or meridional winds, and what are the associated thermodynamic features? These and other questions are being addressed in present research and will further demonstrate the value of the SIPAM network dataset.

Acknowledgments. This research has been funded by the Fundação de Amparo à Pesquisa do Estado de São Paulo (FAPESP) (Grants 2009/15235-8, 2013/105014-0) and is part of a Ph.D. thesis. It was also partially funded by the Coordenação de Aperfeiçoamento de Pessoal de Nível Superior (CAPES), Conselho Nacional de Desenvolvimento Científico e Tecnológico (CNPq), and Ministério da Defesa proposals PTA-SG/2014_6.4. We

thank Sistema de Proteção da Amazônia (SIPAM) for providing the weather radar dataset and facilitating this study.

REFERENCES

- Albrecht, R. I., and M. A. F. Silva Dias, 2005: Microphysical evidence of the transition between predominant convective/stratiform rainfall associated with the intraseasonal oscillation in the southwest Amazon. *Acta Amazonica*, **35**, 175–184, doi:10.1590/S0044-59672005000200007.
- , C. A. Morales, and M. A. F. Silva Dias, 2011: Electrification of precipitating systems over the Amazon: Physical processes of thunderstorm development. *J. Geophys. Res.*, **116**, D08209, doi:10.1029/2010JD014756.
- Alcântara, C. R., M. A. F. Silva Dias, E. P. Souza, and J. C. P. Cohen, 2011: Verification of the role of the low level jets in Amazon squall lines. *Atmos. Res.*, **100**, 36–44, doi:10.1016/j.atmosres.2010.12.023.
- Anagnostou, E. N., and W. F. Krajewski, 1997: Simulation of radar reflectivity fields: Algorithm formulation and evaluation. *Water Resour. Res.*, **33**, 1419–1428, doi:10.1029/97WR00233.
- , and C. A. Morales, 2002: Rainfall estimation from TOGA radar observations during LBA field campaign. *J. Geophys. Res.*, **107**, 8068, doi:10.1029/2001JD000377.
- , —, and T. Dinku, 2001: The use of TRMM precipitation radar observations in determining ground radar calibration biases. *J. Atmos. Oceanic Technol.*, **18**, 616–628, doi:10.1175/1520-0426(2001)018<0616:TUOTPR>2.0.CO;2.
- Andreae, M. O., D. Rosenfeld, P. Artaxo, A. A. Costa, G. P. Frank, K. M. Longo, and M. A. F. Silva Dias, 2004: Smoking rain clouds over the Amazon. *Science*, **303**, 1337–1342, doi:10.1126/science.1092779.
- Andrieu, H., J. D. Creutin, G. Delrieu, and D. Faure, 1997: Use of a weather radar for the hydrology of a mountainous area. Part I: Radar measurement interpretation. *J. Hydrol.*, **193**, 1–25, doi:10.1016/S0022-1694(96)03202-7.
- Artaxo, P., and Coauthors, 2002: Physical and chemical properties of aerosols in the wet and dry seasons in Rondônia, Amazonia. *J. Geophys. Res.*, **107**, 8081, doi:10.1029/2001JD000666.
- Bean, B. R., and E. J. Dutton, 1968: *Radio Meteorology*. Dover Publications Inc., 417 pp.
- Bech, J., B. Codina, J. Lorente, and D. Bebbington, 2003: The sensitivity of single polarization weather radar beam blockage correction to variability in the vertical refractivity gradient. *J. Atmos. Oceanic Technol.*, **20**, 845–855, doi:10.1175/1520-0426(2003)020<0845:TSOSPW>2.0.CO;2.
- Bechtold, P., J.-P. Chaboureaud, A. Beljaars, A. K. Betts, M. Köhler, M. Müller, and J.-L. Redelsperger, 2004: The simulation of the diurnal cycle of convective precipitation over land in a global model. *Quart. J. Roy. Meteor. Soc.*, **130**, 3119–3137, doi:10.1256/qj.03.103.
- Buarque, D. C., R. C. D. de Paiva, R. T. Clarke, and C. A. B. Mendes, 2011: A comparison of Amazon rainfall characteristics derived from TRMM, CMORPH and the Brazilian national rain gauge network. *J. Geophys. Res.*, **116**, D19105, doi:10.1029/2011JD016060.
- Carvalho, L. M. V., C. Jones, and M. A. F. Silva Dias, 2002: Intraseasonal large-scale circulations and mesoscale convective activity in tropical South America during the TRMM-LBA campaign. *J. Geophys. Res.*, **107**, 8042, doi:10.1029/2001JD000745.

- Cifelli, R., W. A. Petersen, L. D. Carey, S. A. Rutledge, and M. A. F. Silva Dias, 2002: Radar observations of the kinematic, microphysical, and precipitation characteristics of two MCSs in TRMM LBA. *J. Geophys. Res.*, **107**, 8077, doi:10.1029/2000JD000264.
- Cohen, J. C. P., M. A. F. Silva Dias, and C. A. Nobre, 1995: Environmental conditions associated with Amazonian squall lines: A case study. *Mon. Wea. Rev.*, **123**, 3163–3174, doi:10.1175/1520-0493(1995)123<3163:ECAWAS>2.0.CO;2.
- , D. R. Fitzjarrald, F. A. F. D'Oliveira, I. Saraiva, I. R. S. Barbosa, A. W. Gandu, and P. A. Kuhn, 2014: Radar-observed spatial and temporal rainfall variability near the Tapajós-Amazon confluence. *Rev. Bras. Meteor.*, **29**, 23–30, doi:10.1590/0102-778620130058.
- De Oliveira, A. P., and D. R. Fitzjarrald, 1993: The Amazon river breeze and the local boundary layer: I. Observations. *Bound.-Layer Meteor.*, **63**, 141–162, doi:10.1007/BF00705380.
- Dos Santos, M. J., M. A. F. Silva Dias, and E. D. Freitas, 2014: Influence of local circulations on wind, moisture, and precipitation close to Manaus City, Amazon Region, Brazil. *J. Geophys. Res.*, **119**, 13 233–13 249, doi:10.1002/2014JD021969.
- Doviak, R. J., and D. S. Zrnić, 1993: *Doppler Radar and Weather Observations*. 2nd ed. Academic Press, 562 pp.
- Figueroa, S. N., and C. A. Nobre, 1990: Precipitations distribution over central and western tropical South America. *Climanálise*, **5**, 36–45.
- Greco, S., and Coauthors, 1990: Rainfall and surface kinematic conditions over central Amazonia during ABLE 2B. *J. Geophys. Res.*, **95**, 17 001–17 014, doi:10.1029/JD095iD10p17001.
- Hamilton, M. G., and J. R. Tarifa, 1978: Synoptic aspects of a polar outbreak leading to frost in tropical Brazil, July 1972. *Mon. Wea. Rev.*, **106**, 1545–1556, doi:10.1175/1520-0493(1978)106<1545:SAOAO>2.0.CO;2.
- Herdies, D. L., A. da Silva, M. A. F. Silva Dias, and R. N. Ferreira, 2002: Moisture budget of the bimodal pattern of the summer circulation over South America. *J. Geophys. Res.*, **107**, 8075, doi:10.1029/2001JD000997.
- Iguchi, T., and R. Meneghini, 1994: Intercomparison of single-frequency methods for retrieving a vertical rain profile from airborne or spaceborne radar data. *J. Atmos. Oceanic Technol.*, **11**, 1507–1516, doi:10.1175/1520-0426(1994)011<1507:IOSFMF>2.0.CO;2.
- Kitchen, M., and R. M. Blackall, 1992: Representativeness errors in comparisons between radar and gauge measurements of rainfall. *J. Hydrol.*, **134**, 13–33, doi:10.1016/0022-1694(92)90026-R.
- Kulie, M. S., M. Robinson, D. A. Marks, B. S. Ferrier, D. Rosenfeld, and D. B. Wolff, 1999: Operational processing of ground validation data for the Tropical Rainfall Measuring Mission. Preprints, *29th Int. Conf. on Radar Meteorology*, Montreal, QC, Canada, Amer. Meteor. Soc., 736–739.
- Kummerow, C., W. Barnes, T. Kozu, J. Shiue, and J. Simpson, 1998: The Tropical Rainfall Measuring Mission (TRMM) sensor package. *J. Atmos. Oceanic Technol.*, **15**, 809–817, doi:10.1175/1520-0426(1998)015<0809:TTRMMT>2.0.CO;2.
- Lang, T. J., S. W. Nesbitt, and L. D. Carey, 2009: On the correction of partial beam blockage in polarimetric radar data. *J. Atmos. Oceanic Technol.*, **26**, 943–957, doi:10.1175/2008JTECHA1133.1.
- Lee, A. C. L., 1986: An experimental study of the remote location of lightning flashes using a VLF arrival time difference technique. *Quart. J. Roy. Meteor. Soc.*, **112**, 203–229, doi:10.1002/qj.49711247112.
- Liu, C., E. J. Zipser, D. J. Cecil, S. W. Nesbitt, and S. Sherwood, 2008: A cloud and precipitation feature database from nine years of TRMM observations. *J. Appl. Meteor. Climatol.*, **47**, 2712–2728, doi:10.1175/2008JAMC1890.1.
- Longo, M., R. De Camargo, and M. A. F. Silva Dias, 2004: Análise das características dinâmicas e sinóticas de um evento de friagem durante a estação chuvosa no sudoeste da Amazônia. *Rev. Bras. Meteor.*, **19**, 59–72. [Available online at http://www.rbmet.org.br/port/revista/revista_artigo.php?id_artigo=43.]
- Machado, L. A. T., W. B. Rossow, R. L. Guedes, and A. W. Walker, 1998: Life cycle variations of mesoscale convective systems over the Americas. *Mon. Wea. Rev.*, **126**, 1630–1654, doi:10.1175/1520-0493(1998)126<1630:LCVOMC>2.0.CO;2.
- , and Coauthors, 2014: The CHUVA project: How does convection vary across Brazil? *Bull. Amer. Meteor. Soc.*, **95**, 1365–1380, doi:10.1175/BAMS-D-13-00084.1.
- Maddox, R. A., J. Zhang, J. J. Gourley, and K. W. Howard, 2002: Weather radar coverage over the contiguous United States. *Wea. Forecasting*, **17**, 927–934, doi:10.1175/1520-0434(2002)017<0927:WRCOTC>2.0.CO;2.
- Malkomes, M., F. Fukuda, F. Rocheleau, and J. Werner, 2002: The SIVAM project: Weather radar network for the Amazon region. *Proc. Second European Conf. on Radar in Meteorology and Hydrology*, Delft, Netherlands, European Conference on Radar in Meteorology and Hydrology, 331–334. [Available online at <http://copernicus.org/erad/online/erad-331.pdf>.]
- Marengo, J. A., C. A. Nobre, and A. D. Culf, 1997: Climatic impacts of “friagens” in forested and deforested areas of the Amazon basin. *J. Appl. Meteor.*, **36**, 1553–1566, doi:10.1175/1520-0450(1997)036<1553:CIOFIF>2.0.CO;2.
- Martins, J. A., M. A. F. Silva Dias, and F. L. T. Gonçalves, 2009: Impact of biomass burning aerosols on precipitation in the Amazon: A modeling case study. *J. Geophys. Res.*, **114**, D02207, doi:10.1029/2007JD009587.
- Mohr, K. I., J. S. Famiglietti, and E. J. Zipser, 1999: The contribution to tropical rainfall with respect to convective system type, size, and intensity estimated from the 85-GHz ice-scattering signature. *J. Appl. Meteor.*, **38**, 596–606, doi:10.1175/1520-0450(1999)038<0596:TCTTRW>2.0.CO;2.
- Molion, L. C. B., 1987: Climatologia dinâmica da região Amazônica: Mecanismos de precipitação. *Rev. Bras. Meteor.*, **2**, 107–117.
- Morales, C. A., J. R. Neves, and E. Anselmo, 2011: Sferics Timing and Ranging Network—STARNET: Evaluation over South America. *Proc. 14th Int. Conf. on Atmospheric Electricity*, Rio de Janeiro, Brazil, International Association of Meteorology and Atmospheric Sciences, 4 pp.
- Negri, A. J., R. F. Adler, E. J. Nelkin, and G. J. Huffman, 1994: Regional rainfall climatologies derived from Special Sensor Microwave Imager (SSM/I) data. *Bull. Amer. Meteor. Soc.*, **75**, 1165–1182, doi:10.1175/1520-0477(1994)075<1165:RRCDFS>2.0.CO;2.
- , L. Xu, and R. F. Adler, 2002: A TRMM-calibrated infrared rainfall algorithm applied over Brazil. *J. Geophys. Res.*, **107**, 8048, doi:10.1029/2000JD000265.
- Nesbitt, S. W., and E. J. Zipser, 2003: The diurnal cycle of rainfall and convective intensity according to three years of TRMM measurements. *J. Climate*, **16**, 1456–1475, doi:10.1175/1520-0442-16.10.1456.
- Oliveira, A. S., 1986: Interações entre sistemas frontais na América do Sul e a convecção da Amazônia. Dissertação de Mestrado,

- Dept. de Meteorologia, Instituto Nacional de Pesquisas Espaciais, 246 pp.
- Parmenter, F. C., 1976: A Southern Hemisphere cold front passage at the equator. *Bull. Amer. Meteor. Soc.*, **57**, 1435–1440, doi:10.1175/1520-0477(1976)057<1435:ASHCFP>2.0.CO;2.
- Petersen, W. A., and S. A. Rutledge, 2001: Regional variability in tropical convection: Observations from TRMM. *J. Climate*, **14**, 3566–3586, doi:10.1175/1520-0442(2001)014<3566:RVITCO>2.0.CO;2.
- , S. W. Nesbitt, R. J. Blakeslee, R. Cifelli, P. Hein, and S. A. Rutledge, 2002: TRMM observations of intraseasonal variability in convective regimes over the Amazon. *J. Climate*, **15**, 1278–1294, doi:10.1175/1520-0442(2002)015<1278:TOOIVI>2.0.CO;2.
- Rao, V. B., and K. Hada, 1990: Characteristics of rainfall over Brazil: Annual variations and connections with the Southern Oscillation. *Theor. Appl. Climatol.*, **42**, 81–91, doi:10.1007/BF00868215.
- Rickenbach, T. M., 2004: Nocturnal cloud systems and the diurnal variation of clouds and rainfall in southwestern Amazonia. *Mon. Wea. Rev.*, **132**, 1201–1219, doi:10.1175/1520-0493(2004)132<1201:NCSATD>2.0.CO;2.
- , R. N. Ferreira, J. B. Halverson, D. L. Herdies, and M. A. F. Silva Dias, 2002: Modulation of convection in the southwestern Amazon basin by extratropical stationary fronts. *J. Geophys. Res.*, **107**, doi:10.1029/2000JD000263.
- Rosenfeld, D., and M. A. F. Silva Dias, 2008: Can the slowing of auto-conversion result in increasing precipitation? *iLEAPS Newsletter*, No. 5, International Geosphere-Biosphere Programme, Stockholm, Sweden, 30–33.
- , E. Amitai, and D. B. Wolff, 1995: Classification of rain regimes by the three-dimensional properties of reflectivity fields. *J. Appl. Meteor.*, **34**, 198–211, doi:10.1175/1520-0450(1995)034<0198:CORRBT>2.0.CO;2.
- Rowe, A. K., and R. A. Houze Jr., 2014: Microphysical characteristics of MJO convection over the Indian Ocean during DYNAMO. *J. Geophys. Res.*, **119**, 2543–2554, doi:10.1002/2013JD020799.
- Saad, S. I., H. R. da Rocha, M. A. F. Silva Dias, and R. Rosolem, 2010: Can the deforestation breeze change the rainfall in Amazonia? A case study for the BR-163 highway region. *Earth Interact.*, **14**, doi:10.1175/2010EI351.1.
- Saraiva, I., 2010: Características dos sistemas precipitantes observados via radar meteorológico de Manaus. Dissertação de Mestrado, Dept. de Ciências Atmosféricas, Universidade de São Paulo, 139 pp. [Available online at http://www.iag.usp.br/pos/sites/default/files/m_ivan_saraiva.pdf.]
- Satyamurty, P., C. A. Nobre, and P. L. Silva Dias, 1998: South America. *Meteorology of the Southern Hemisphere*, *Meteor. Monogr.*, No. 49, Amer. Meteor. Soc., 119–139.
- Scarchilli, G., E. Gorgucci, D. Giuli, L. Baldini, L. Facheris, and E. Palmisano, 1995: Weather radar calibration by means of the metallic sphere and multiparameter radar measurements. *Nuovo Cimento*, **18C**, 57–70, doi:10.1007/BF02561459.
- Silva Dias, M. A. F., and Coauthors, 2002: Clouds and rain processes in a biosphere-atmosphere interaction context in the Amazon region. *J. Geophys. Res.*, **107**, 8072, doi:10.1029/2001JD000335.
- , P. L. Silva Dias, M. Longo, D. R. Fitzjarrald, and A. S. Denning, 2004: River breeze circulation in eastern Amazonia: Observations and modelling results. *Theor. Appl. Climatol.*, **78**, 111–121, doi:10.1007/s00704-004-0047-6.
- , R. Avissar, and P. Silva Dias, 2009a: Modeling the regional and remote climatic impact of deforestation. *Amazonia and Global Change, Geophys. Monogr.*, Vol. 186, Amer. Geophys. Union, 251–260, doi:10.1029/2008GM000778.
- , J. R. Rozante, and L. A. T. Machado, 2009b: Complexos convectivos de mesoescala na América do Sul. *Tempo e Clima no Brasil*. I. F. A. Cavalcanti et al., Eds., Oficina de Textos, 181–191.
- Steiner, M., R. A. Houze Jr., and S. E. Yuter, 1995: Climatological characterization of three-dimensional storm structure from operational radar and rain gauge data. *J. Appl. Meteor.*, **34**, 1978–2007, doi:10.1175/1520-0450(1995)034<1978:CCOTDS>2.0.CO;2.
- Ter Steege, H., and Coauthors, 2013: Hyperdominance in the Amazonian tree flora. *Science*, **342**, doi:10.1126/science.1243092.
- Vera, C., and Coauthors, 2006: Toward a unified view of the American monsoon systems. *J. Climate*, **19**, 4977–5000, doi:10.1175/JCLI3896.1.
- Westrick, K. J., C. F. Mass, and B. A. Colle, 1999: The limitations of the WSR-88D radar network for quantitative precipitation measurement over the coastal western United States. *Bull. Amer. Meteor. Soc.*, **80**, 2289–2298, doi:10.1175/1520-0477(1999)080<2289:TLOTWR>2.0.CO;2.
- Williams, E., and Coauthors, 2002: Contrasting convective regimes over the Amazon: Implications for cloud electrification. *J. Geophys. Res.*, **107**, 8082, doi:10.1029/2001JD000380.
- Yuter, S. E., and R. A. Houze Jr., 1995: Three-dimensional kinematic and microphysical evolution of Florida cumulonimbus. Part II: Frequency distributions of vertical velocity, reflectivity, and differential reflectivity. *Mon. Wea. Rev.*, **123**, 1941–1963, doi:10.1175/1520-0493(1995)123<1941:TDKAME>2.0.CO;2.
- Zeng, Z., S. E. Yuter, R. A. Houze Jr., and D. E. Kingsmill, 2001: Microphysics of the rapid development of heavy convective precipitation. *Mon. Wea. Rev.*, **129**, 1882–1904, doi:10.1175/1520-0493(2001)129<1882:MOTRDO>2.0.CO;2.